remote sensing

MDPI

Article

Polar Mesospheric Cloud Detections by TROPOMI/Sentinel-5P: First Results and Validation

Weichao Wu [1], Shengyang Gu [1,2,*], Yafei Wei [1], Zhe Wang [1], Yusong Qin [1], Xiuqing Hu [3] and Yongmei Wang [4]

[1] School of Earth and Space Science and Technology, Wuhan University, Wuhan 430072, China; weosuper@whu.edu.cn (W.W.); weiyafei@whu.edu.cn (Y.W.); 2025102120016@whu.edu.cn (Z.W.); qinyusong@whu.edu.cn (Y.Q.)
[2] Wuhan Institute of Quantum Technology, Wuhan 430205, China
[3] Chinese Academy of Meteorological Sciences, Beijing 100081, China; huxq@cma.gov.cn
[4] Laboratory of Space Environment Exploration, National Space Science Center, Beijing 100190, China; wym@nssc.ac.cn
* Correspondence: gushengyang@whu.edu.cn

Highlights

What are the main findings?

- We present the first systematic detection of polar mesospheric clouds using TROPOMI ultraviolet observations and an improved SBUV-type retrieval algorithm adapted to UV1 measurements.
- Validation against CIPS and OMPS-NP shows that TROPOMI captures large-scale PMC structures consistently while resolving finer-scale features that are difficult to detect with lower-resolution sensors.

What are the implications of the main findings?

- TROPOMI can help bridge the gap between long-term coarse-resolution PMC records and high-resolution observations, extending observational capability after the end of AIM/CIPS operations.
- The dataset provides new observational support for studies of mesospheric dynamics, including small-scale variability and possible planetary-wave-related modulation of PMC activity.

Abstract

We present the first results of polar mesospheric cloud (PMC) detection using ultraviolet observations from TROPOMI (TROPOspheric Monitoring Instrument). An improved retrieval algorithm, developed on the basis of the SBUV-type approach and adapted to TROPOMI UV1 (270–300 nm) measurements, combines spatial binning, iterative Rayleigh background modeling, and adaptive thresholding to extract PMC signals from the background atmosphere. The robustness of the TROPOMI retrievals is evaluated through multi-scale comparisons with PMC data from the Cloud Imaging and Particle Size experiment (CIPS) and the Ozone Mapping and Profiler Suite Nadir Profiler (OMPS-NP). Compared with CIPS, the two datasets show broadly consistent hemispheric-scale horizontal structures and a westward wave-like phase progression consistent with possible quasi-5-day planetary-wave modulation, despite local-time differences. Compared with OMPS-NP, residual albedo under matched spatiotemporal conditions shows strong agreement for bright PMCs, whereas differences in spatial resolution lead to discrepancies in the detection of faint clouds. Seasonal-scale comparisons of PMC occurrence frequency also show consistent variability among the datasets. These results demonstrate that TROPOMI can resolve

Check for updates

Academic Editor: Matthew McGill

Received: 4 April 2026
Revised: 10 May 2026
Accepted: 13 May 2026
Published: 16 May 2026

Copyright: © 2026 by the authors. Licensee MDPI, Basel, Switzerland. This article is an open access article distributed under the terms and conditions of the Creative Commons Attribution (CC BY) license.

PMC structures smaller than 250 km that are difficult to detect with current low-resolution instruments. TROPOMI therefore provides a bridge between long-term coarse-resolution records and high-resolution observations, offering valuable data for studies of mesospheric dynamics and climate change.

Keywords: polar mesospheric clouds; satellite remote sensing; TROPOMI; ultraviolet detection

1. Introduction

Polar mesospheric clouds (PMCs), commonly referred to as noctilucent clouds (NLCs) when observed from the ground, are the highest clouds in Earth's atmosphere. They typically form in summer at high latitudes (>50°) near the mesopause, at an altitude of approximately 83 km, and exhibit extremely low optical thickness (<10^{-4}). These ice clouds are sensitive to temperature and water vapor and are therefore widely regarded as indicators of mesospheric climate variability [1]. Observational evidence suggests that PMC occurrence frequency and brightness have increased over recent decades, with reported trends of approximately 5% per decade [2], together with a gradual expansion toward lower latitudes [3,4]. These observations highlight the sensitivity of PMCs to global change and their relevance to climate research [5–7].

Satellite remote sensing has been the primary tool for investigating PMC spatial distribution, seasonal evolution, and long-term variability since the first daytime observations by OGO-6 in 1969 [8]. Existing satellite observations can be broadly categorized into four measurement geometries: (1) limb scattering, (2) ultraviolet nadir backscattering, (3) solar occultation, and (4) thermal emission. Limb-scattering instruments (e.g., OSIRIS [9], SCIAMACHY [10], and OMPS-LP [11]) offer the highest sensitivity to PMCs. They resolve vertical structure and brightness variations and are primary data sources for seasonal and zonal studies. Ultraviolet nadir backscattering instruments (SBUV [12], SBUV/2 [13], OMI [14], and OMPS-NP [15]) provide near-global daily coverage and are particularly suitable for studies of horizontal distributions and long-term trends. Solar occultation instruments (e.g., HALOE [16] and SOFIE [17]) provide excellent vertical resolution (<1 km) but limited sampling and latitude coverage, which restrict large-scale studies of horizontal PMC distribution. Short-duration thermal infrared observations (CRISTA [18] and SPIRIT III [19]) mainly constrain the radiative properties of ice particles.

Limb sounders and lidars have provided detailed knowledge of the vertical structure and microphysics of PMCs [20,21]. However, horizontal resolutions of hundreds of kilometers and the sparse distribution of ground-based sites limit our understanding of small-scale horizontal morphology. The Solar Backscattered Ultraviolet instruments (SBUV) onboard NOAA (National Oceanic and Atmospheric Administration) satellites have established a multi-solar-cycle PMC dataset [22–24], but its spatial resolution, coarser than about 170 km × 170 km, cannot resolve finer small-scale PMC structures. In 2007, CIPS onboard the Aeronomy of Ice in the Mesosphere (AIM) satellite was launched with unprecedented spatial resolution (7.5 km × 7.5 km), substantially advancing research on PMC microphysics, mesospheric dynamics, and climate coupling [25–28]. PMCs as indicators of environmental change have since been further validated [29–31]. Unfortunately, battery anomalies ended CIPS operations in March 2023, leaving a critical gap in high-resolution PMC observations.

To extend PMC observing capability, DeLand et al. [14] and Langowski et al. [32] adapted SBUV-type algorithms to OMI and SCIAMACHY, respectively, demonstrating the feasibility of PMC detection from nadir-viewing ultraviolet spectrometers. However, row

anomalies in OMI [33] and the termination of the SCIAMACHY mission limit the long-term utility of these datasets. There is therefore a clear need for a new sensor that combines high spatial resolution, stable radiometric calibration, and global coverage. The TROPOMI instrument on Sentinel-5P offers this opportunity, with strong ultraviolet signal-to-noise ratio in the 270–300 nm range, spatial resolution up to 7 km × 28 km, and daily global coverage [34], thereby filling the gap between long-term SBUV records and high-resolution CIPS observations.

Here, we present the first systematic PMC detection using TROPOMI data. We adapt and extend the SBUV-type algorithm to the characteristics of the instrument and validate the retrieval against CIPS and OMPS-NP. We further analyze PMC variability at orbital, daily, and seasonal timescales. This study demonstrates the potential of TROPOMI for high-resolution PMC detection and provides data support for studies of the mesospheric atmosphere.

2. Materials and Methods

2.1. Data

2.1.1. Sentinel-5P/TROPOMI

TROPOMI is a new-generation push-broom imaging spectrometer in Sun-synchronous polar orbit, launched in 2017 on Sentinel-5P at an altitude of about 824 km with an ascending-node local time of 13:30 [34]. TROPOMI operates in nadir mode and measures Earth radiance from 270 to 2385 nm at a spectral resolution of 0.3–0.5 nm using a two-dimensional detector, with a cross-track swath of about 2600 km (Figure 1a). Building on the heritage of the Ozone Monitoring Instrument (OMI), which onboard Aura satellite and launched in 2004, TROPOMI achieves major improvements in spatial resolution and signal-to-noise ratio. This study employs the TROPOMI L1B ultraviolet radiance product (L1B_RA_BD1) and solar irradiance product (L1B_IR_UVN), version 02.01.00, both of which provide measured radiance/irradiance data within the UV1 band (270–300 nm) at a spectral resolution of approximately 0.065 nm.

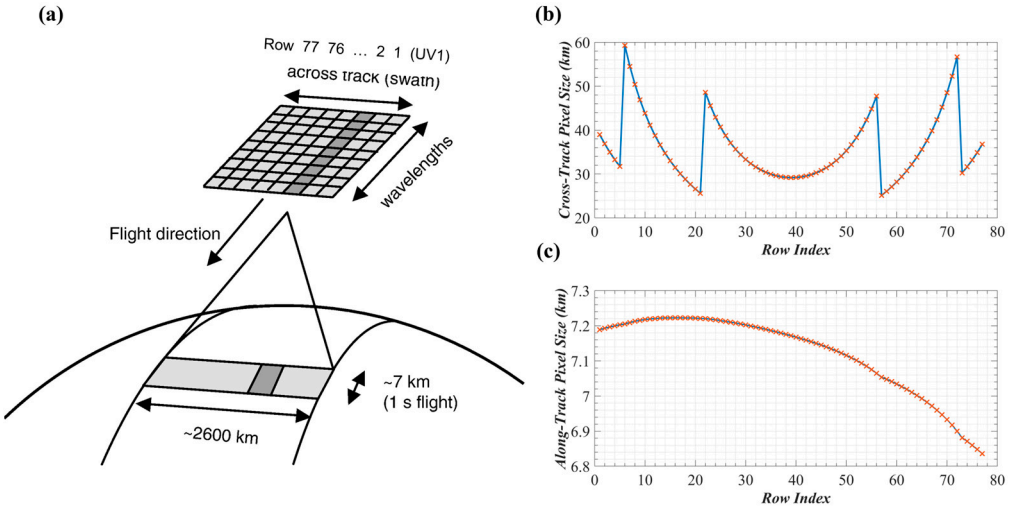


Figure 1. (**a**) TROPOMI measurement principle, adapted from Veefkind et al. [34]. (**b**) Cross-track pixel size of TROPOMI UV1 data at 60°N on 29 June 2018, calculated from the L1B geolocation information. (**c**) Along-track pixel size calculated from the same geolocation data.

Note that the cross-track pixel size of TROPOMI varies with pixel location in the cross-track direction (Figure 1b). TROPOMI applies an adaptive pixel binning strategy in cross-track direction to improve the signal-to-noise ratio and make the cross-track pixel sizes more uniform [35]. For example, the UV1 data are binned into 77 cross-track pixels,

with a binning factor of 16 for pixels near nadir (rows 22–56), 8 for pixels in the intermediate region (rows 6–21 and 57–72), and 4 for pixels at the edges of the swath (rows 1–5 and 73–77). As a result, the cross-track pixel size varies smoothly within each binning group but shows jumps near the transition between different groups. In the along-track direction, the pixel size is approximately 7 km (Figure 1c). Since 6 August 2019, the TROPOMI imaging interval has been reduced from 1080 to 840 ms, decreasing the along-track pixel size to approximately 5.5 km. All TROPOMI data used in this study were quality screened according to the official documentation [36], and all pixels affected by instrument anomalies were removed.

2.1.2. AIM/CIPS

The Cloud Imaging and Particle Size (CIPS) instrument is dedicated to PMC observations and consists of four wide-field cameras that use narrowband filters and ultraviolet imagers at 265 nm [37]. CIPS was launched on the AIM satellite in 2007 into a near-polar Sun-synchronous orbit at an altitude of about 600 km with a descending-node local time of 12:00. Its nadir resolution is 5 km × 5 km. CIPS completes about 14 orbits per day and covers the polar cap from 55° to 87° latitude.

We use CIPS Level 3A (v5.20) data to validate the TROPOMI retrievals. CIPS L3A has a spatial resolution of 7.5 km × 7.5 km over the hemisphere poleward of 50° and provides zenith PMC albedo.

2.1.3. S-NPP/OMPS-NP

The Ozone Mapping and Profiler Suite Nadir Profiler (OMPS-NP) is an ozone profiler that provides global ozone profiles and related upper-atmosphere information and was designed to maintain consistency with the SBUV/2 record [38]. It has flown on the Suomi National Polar-orbiting Partnership (S-NPP) satellite since 2011 in a Sun-synchronous orbit near 824 km altitude with an ascending-node local time near 13:30. OMPS-NP covers approximately 250–310 nm at a spectral resolution of about 0.6 nm, and the ground footprint is approximately 250 km × 250 km per pixel.

Sentinel-5P and S-NPP have similar orbits, enabling TROPOMI and OMPS-NP to observe the same region within about five minutes. This excellent spatiotemporal coincidence allows direct comparison. We use OMPS-NP PMC data from DeLand et al. [15], which provide PMC albedo at 252.0, 273.5, and 283.1 nm.

2.2. Methods

To achieve robust PMC detection from TROPOMI, we implement an improved SBUV-type algorithm with three main components:

1. Spectral preprocessing and optimized wavelength selection;
2. Rayleigh background modeling and iterative cloud masking;
3. Multi-criterion PMC detection.

2.2.1. Spectral Preprocessing and Noise Reduction

TROPOMI provides rich spectral information, but redundancy between adjacent channels and additional noise can obscure the PMC signal [39]. We therefore select wavelengths according to PMC microphysics.

Following common models, PMCs are treated as ice clouds composed of randomly oriented oblate spheroids with an axis ratio of 2 [40]. Equivalent-sphere radii range from 20 to 100 nm with a Gaussian size distribution whose width varies with radius. Using T-matrix theory [41–43], we calculate scattering cross-sections for particle radii from 20 to 80 nm (Figure 2a). Results show that scattering intensity increases toward shorter

wavelengths, favoring shortwave detection. However, shorter channels also have lower measured radiance and albedo (Figure 2b,d), making weak signals more susceptible to noise. Bak et al. [44] reported significant temporal drift in TROPOMI UV1 spectra below 280 nm. Considering the signal-to-noise ratio above 280 nm (Figure 2e), we adopt five diagnostic wavelengths: 283.0, 287.0, 291.5, 295.0, and 298.0 nm. All pixels are linearly interpolated to these bands, and albedo (Figure 2d) is calculated by dividing radiance (Figure 2b) by solar irradiance (Figure 2c). Before interpolation, we apply a 1 × 49 spectral window (~3 nm) moving average along the wavelength dimension to suppress noise.

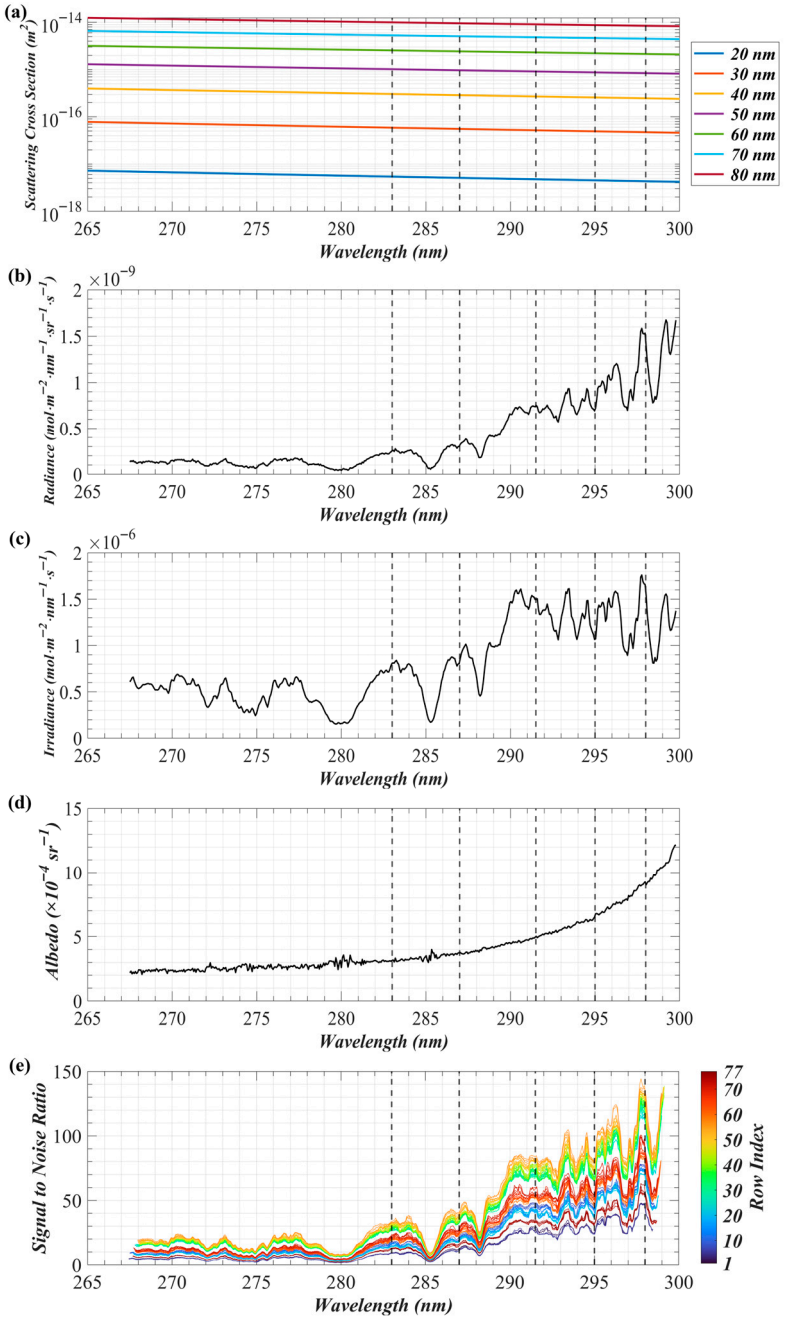


Figure 2. (**a**) Scattering cross-section of ice particles with radii from 20 to 80 nm over 265–300 nm; (**b**) TROPOMI UV1 radiance spectrum at 60.4°N, 20.5°E for orbit 03675 on 29 June 2018; (**c**) solar irradiance spectrum for the same orbit; (**d**) corresponding albedo spectrum; (**e**) mean signal-to-noise ratio for each row of orbit 03675. Black dashed lines indicate the selected wavelengths 195 (283.0, 287.0, 291.5, 295.0, 298.0 nm).

We further improve the signal-to-noise ratio through spatial binning. All data are downsampled using a 2 × 2 window. Rows 1–5 and 73–77 are excluded because of low SNR (<10) near the swath edges. For the nadir cluster (rows 38–40), a 2 × 3 (along-track × cross-track) window is used to preserve the relative position of the center pixel. Because cross-track pixel ground footprints differ (Figure 1b,c), a simple arithmetic mean of albedo would bias the merged values. We therefore weight albedo by each pixel's ground-projected instantaneous field-of-view area during binning, computed separately for each wavelength (Equation (1)).

$$Alb_bin_i(\lambda) = \sum_{j=1}^{n} \frac{S(j)}{S_{total}} \cdot Alb(j, \lambda) \quad (1)$$

where $S(j)$ is the ground-projected area of pixel j (along-track size multiplied by cross-track size), S_{total} is the sum of the areas of valid pixels within the window, $Alb(j, \lambda)$ is the albedo of pixel j at wavelength λ, and $Alb_bin_i(\lambda)$ is the binned albedo for bin i. Valid pixels are those that pass the quality screening described in Section 2.1.1. After binning, the cross-track dimension is reduced from 77 to 33 pixels; the corresponding row mapping is listed in Table 1.

Table 1. Pixel row numbers of TROPOMI UV1 data before and after binning. Pixels in rows 1–5 and 73–77 are excluded because of low signal-to-noise ratio. '. . .' stands for the ellipsis, as the row numbers change in a certain pattern.

Before Binning	After Binning
6, 7	1
. . .	. . .
20, 21	8
22, 23	9
. . .	. . .
38, 39, 40 (Nadir point)	17
. . .	. . .
55, 56	25
57, 58	26
. . .	. . .
71, 72	33

2.2.2. Rayleigh Background Modeling

The basic mode of TROPOMI's PMC detection is illustrated in Figure 3. During operation, the radiation measured by the TROPOMI detector consists of the radiation scattered by PMCs (R_{PMC}) and the Rayleigh scattering radiation from the background atmosphere (R_{Ray}). The optically thin nature of PMCs makes the radiation they scatter extremely weak compared to the total solar radiation (R_{solar}). However, due to the strong absorption by ozone molecules in the Earth's atmosphere, most ultraviolet (<300 nm) radiation is absorbed by ozone molecules (R_{ozone}). Only a very small portion of ultraviolet radiation is scattered into outer space by high-altitude atmospheric molecules in the form of Rayleigh scattering, and then captured by the detector. This process maximizes the contrast between cloud scattering and Rayleigh scattering from the background atmosphere, enabling cloud scattering to be distinguished, as shown in Figure 3.

The total albedo measured by the detector can be expressed as the sum of PMC albedo and Rayleigh albedo. Because PMC ice particles have extremely small optical thickness, the contribution of multiple scattering to radiative transfer can be neglected [40,45]. We therefore adopt the single-scattering approximation to simplify the radiative transfer process [24,40,46].

$$A_{meas}(\theta, \Phi, \varphi, \lambda) = A_{PMC}(\theta, \Phi, \varphi, \lambda) + A_{Ray}(\theta, \Phi, \varphi, \lambda) \quad (2)$$

θ, Φ, and φ denote the satellite viewing angle, scattering angle, and solar zenith angle, respectively. A_{meas}, A_{PMC}, and A_{Ray} denote the measured total albedo, cloud-scattering albedo, and Rayleigh-scattering albedo, respectively. The cloud albedo can therefore be obtained by subtracting the Rayleigh contribution. For each TROPOMI orbit, we use a fourth-order polynomial as a function of solar zenith angle to represent the Rayleigh albedo of the background atmosphere (Figure 4a). The fitting is performed row by row along the cross-track direction to ensure a consistent satellite viewing angle among pixels and to avoid the influence of differences in optical path length on albedo values. Only pixels with latitude greater than 50° and zenith angle less than 85° are used for fitting, and the fitting is carried out separately for each wavelength. After obtaining the fitted values $A_{fit}(\varphi, \lambda)$, we subtract them from the measured albedo $A_{meas}(\lambda)$ to obtain the residual albedo $A_{resid}(\lambda)$ (Figure 4b), which represents potential PMC signals together with measurement noise.

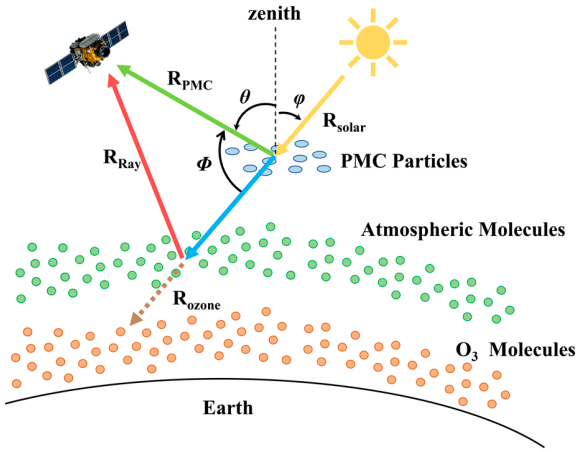


Figure 3. TROPOMI PMC detection principle. θ, Φ, φ denote satellite viewing, scattering, and solar zenith angles, respectively. R_{solar} is the total solar UV radiance. R_{PMC} and R_{Ray} represent UV radiance scattered by PMCs and atmospheric molecules. R_{ozone} is UV radiance absorbed by stratospheric ozone molecules.

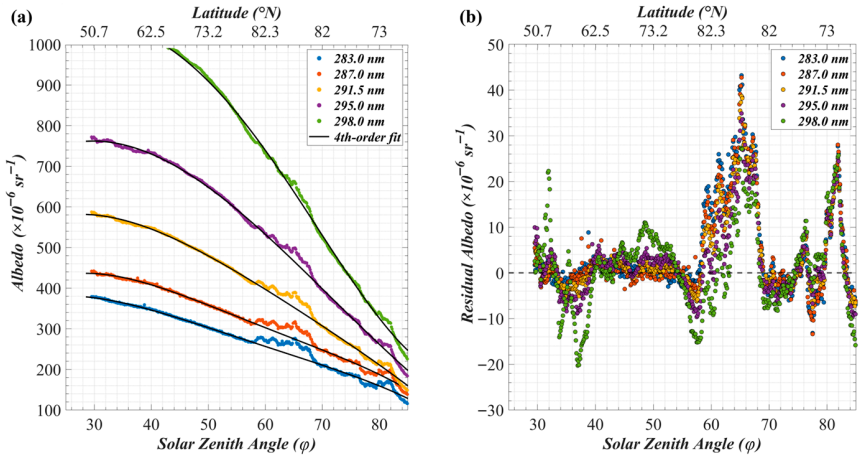


Figure 4. (**a**) Measured albedo variation with solar zenith angle across all wavelengths for all pixels from row 22 (binned) of orbit 03675 on 29 June 2018. Black lines indicate fourth-order fits per wavelength. (**b**) Same as (**a**), but for residual albedo.

When PMCs are present within a TROPOMI orbit, the polynomial fit is inevitably influenced by the cloud signal, causing the fitted Rayleigh albedo to deviate from the true

background. The background-fitting procedure is therefore repeated iteratively. After each iteration, pixels exceeding the PMC detection threshold (discussed in Section 2.2.3) are flagged as cloudy and excluded from the next iteration, so that the fit progressively approaches the ideal Rayleigh background. Based on sensitivity tests, the maximum number of iterations is set to 5.

2.2.3. Multi-Criteria PMC Detection Algorithm

We apply three decision rules to evaluate the residual albedo of each pixel. For a TROPOMI pixel to be identified as a PMC, the residual albedo $A_{resid}(\lambda)$ at different wavelengths must satisfy the following criteria:

1. $A_{resid}(283.0) > 0$, $A_{resid}(287.0) > 0$, $A_{resid}(291.5) > 0$, and $A_{resid}(283.0) > n \times Threshold$, where n is an empirical scaling factor and $Threshold$ is the dynamic PMC detection threshold;
2. $A_{resid}(283.0) > A_{resid}(291.5)$;
3. $k < 0$, where k is the slope of the straight line obtained from a linear fit to the residual albedo values at all wavelengths.

To ensure the reliability of the calculated residuals, we require the residual albedo at the three shortest wavelengths most sensitive to PMCs (283.0, 287.0, and 291.5 nm) to be greater than 0 and the albedo at 283.0 nm, the most sensitive wavelength, to exceed the detection threshold. The theoretical PMC model (Figure 2a) shows that the scattering intensity of PMC ice particles decreases with increasing wavelength. We therefore further constrain the residual albedo by Rules 2 and 3 to ensure that the multi-wavelength residual albedos are consistent with the microphysical characteristics of PMC ice particles. Because 283.0 and 287.0 nm are adjacent wavelengths and both have relatively low SNR (Figure 2e), we do not require the residual albedo at 283.0 nm to exceed that at 287.0 nm. In this study, n is set to 2.2 to balance the false-detection rate against the detection rate for faint PMCs. $Threshold$ refers to the dynamic PMC detection threshold, which is derived from off-season PMC observations and calculated as follows:

First, observations from 10 days before and 10 days after each PMC season (-40 to -31 days and +71 to +80 days) are used as cloud-free background references, and residual albedos are calculated band by band. The data are then partitioned by solar zenith angle using a step of 0.25°, and the albedo variance within each bin is taken as the PMC detection threshold for that zenith-angle range. Because the signal-to-noise ratio and viewing geometry differ among TROPOMI rows, the binned TROPOMI pixels are divided into three groups, rows 1–8, 9–25, and 26–33, and the variance is calculated separately for each group. Finally, a quadratic function is fitted to the bin-wise variance values to obtain a smooth threshold function that varies with solar zenith angle, as shown in Figure 5. At this stage, all pixels whose residual albedo at 283.0 nm exceeds the threshold and whose multi-band albedo is consistent with the physical characteristics of ice crystals are identified as PMCs, and their residual albedos at each wavelength are taken as the corresponding cloud albedos $A_{PMC}(\lambda)$.

2.2.4. Radiometric Angular Normalization

The high spatial resolution of TROPOMI provides a more detailed horizontal structure but also introduces differences in viewing geometry (satellite viewing angle and scattering angle) among pixels. The satellite viewing angle determines the optical path length in the scattering process. At the same time, the anisotropy of light scattering causes systematic differences in the albedo of PMC ice particles at different scattering angles (Figure 6). These differences prevent direct comparison of albedo among pixels with inconsistent viewing geometry. Therefore, after the detection algorithm is applied to all data, the residual albedos

of all identified cloud pixels are normalized to nadir viewing geometry ($\theta = 0°$, $\Phi = 90°$), as shown in Equation (3).

$$A_{Nadir}(\lambda,\ \theta = 0°, \Phi = 90°) = \frac{A_{PMC}(\lambda,\ \theta, \Phi)}{PSF(\Phi, r = 40\ nm)} \cdot \cos\theta \quad (3)$$

where A_{PMC} represents the cloud albedo at each wavelength obtained after threshold-based identification (Section 2.2.3), while A_{Nadir} denotes the nadir-referenced albedo after geometric normalization. θ, Φ, and φ represent the satellite viewing angle, scattering angle, and solar zenith angle, respectively. *PSF* denotes the PMC ice-particle scattering phase function, which depends on particle radius and scattering angle. It is calculated using T-matrix theory (same model parameters as Section 2.2.1), then normalized to a scattering angle of 90° (Figure 6). Owing to the lack of particle-size information, the volume-equivalent spherical radius of all ice particles is fixed at 40 nm [47], and the Gaussian width of the radius distribution is fixed at 15.6 nm [40].

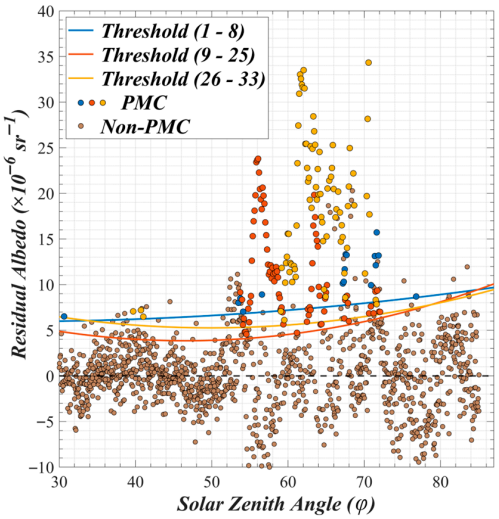


Figure 5. Detection threshold vs. solar zenith angle for various row groups. Colored lines indicate thresholds for different row ranges. Colored and brown circles denote pixels identified as PMCs and non-PMCs, respectively from binned rows 5 (blue), 22 (red), and 29 (yellow) of orbit 03671 on 29 June 2018.

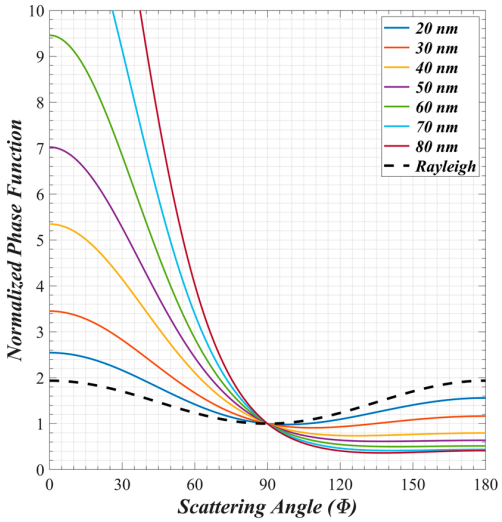


Figure 6. Normalized phase function for PMC ice particles with radii 20–80 nm, with all values normalized to 90° scattering angle.

It should be noted that this normalization corrects the radiometric dependence of PMC albedo on viewing and scattering geometry, but it does not constitute a spatial correction for off-nadir footprint distortion. Off-nadir observations can introduce spatial image distortion through footprint enlargement, footprint-shape deformation, and parallax displacement of high-altitude clouds relative to the ground-projected geolocation. In this study, the footprint-size effect is partly accounted for through geolocation-based area-weighted binning. The remaining spatial distortion mainly affects the apparent position and morphology of small-scale cloud structures, and is therefore considered when interpreting fine-scale comparisons with CIPS.

2.2.5. Spatial Agreement Metrics

To evaluate the spatial consistency between TROPOMI and CIPS PMC detections, both products were mapped onto a common 50 km grid and compared only over grid cells that were valid in both datasets. The main comparison was restricted to 70°N–85°N. Let M_T and M_C denote the binary PMC masks from TROPOMI and CIPS, respectively, where a value of 1 indicates PMC detection and 0 indicates non-detection. For CIPS, PMC occurrence was defined by positive PMC albedo, while the TROPOMI mask was derived from the normalized residual albedo threshold.

The strict grid-cell overlap was quantified using the Intersection over Union (IoU):

$$IoU = \frac{|M_T \cap M_C|}{|M_T \cup M_C|} \tag{4}$$

where $M_T \cap M_C$ represents grid cells identified as PMC by both products, and $M_T \cup M_C$ represents grid cells identified as PMC by either product. *IoU* ranges from 0 to 1, with larger values indicating stronger pixel-level agreement. Days for which no PMC pixels were detected by either product within the common valid domain were treated as undefined for IoU.

Because small spatial offsets may arise from differences in viewing geometry, sampling time, and gridding procedures, we additionally used the Fractions Skill Score (FSS) [48,49] to assess neighborhood-scale morphological agreement. In this study, FSS-3cell denotes FSS computed using a 3 × 3-cell neighborhood on the 50 km grid, corresponding to an approximate spatial scale of 150 km. For each valid grid cell (i, j), the local PMC fraction for data X, where X denotes TROPOMI (T) and CIPS (C), was calculated as

$$f_X(i,j) = \frac{\sum M_X(u,v)V(u,v),\ \ (u,v) \in N_3(i,j)}{\sum V(u,v),\ \ (u,v) \in N_3(i,j)},\ X \in \{T,\ C\} \tag{5}$$

where $N_3(i, j)$ is the 3 × 3-cell neighborhood centered on (i, j), and V(u, v) is the common valid-data mask. The use of V ensures that only grid cells valid in both products contribute to the neighborhood fraction.

The *FSS* was then calculated as

$$FSS = 1 - \frac{\langle (f_T - f_C)^2 \rangle}{\langle {f_T}^2 + {f_C}^2 \rangle} \tag{6}$$

where $\langle \cdot \rangle$ denotes averaging over all common valid grid cells. *FSS* also ranges from 0 to 1, with values closer to 1 indicating stronger agreement in the neighborhood-scale PMC spatial pattern. Compared with IoU, FSS-3cell is less sensitive to one-grid-cell displacement and therefore provides a complementary measure of agreement in the morphology of PMC structures.

3. Results

3.1. TROPOMI PMC Detection Results

Figure 7a presents the TROPOMI PMC detection results for orbit 03675. PMCs are primarily distributed within 70°N–90°N and 90°W–45°E, with the strongest activity near 85°N and 45°W. Figure 7b shows the residual albedos from row 17 of the same orbit. After the background is represented by a fourth-order polynomial and the residual albedo is calculated, PMC pixels show substantially higher residual albedo than background pixels, and the two can be effectively separated using the dynamic threshold. This demonstrates that the proposed method can extract weak PMC signals from strong background scattering. It is noteworthy that some pixels with residual albedo at 283.0 nm exceeding the PMC detection threshold are still classified as cloud-free (Figure 7b), and their number peaks when the zenith angle exceeds 75°. This indicates that these pixels do not satisfy all cloud-identification criteria. As the zenith angle increases, the substantial decrease in ultraviolet radiance and signal-to-noise ratio may cause the residual albedo at 283.0 nm to be anomalously enhanced by measurement noise, thereby leading to an increase in the number of pixels that fail to meet detection criteria and exceed the detection threshold.

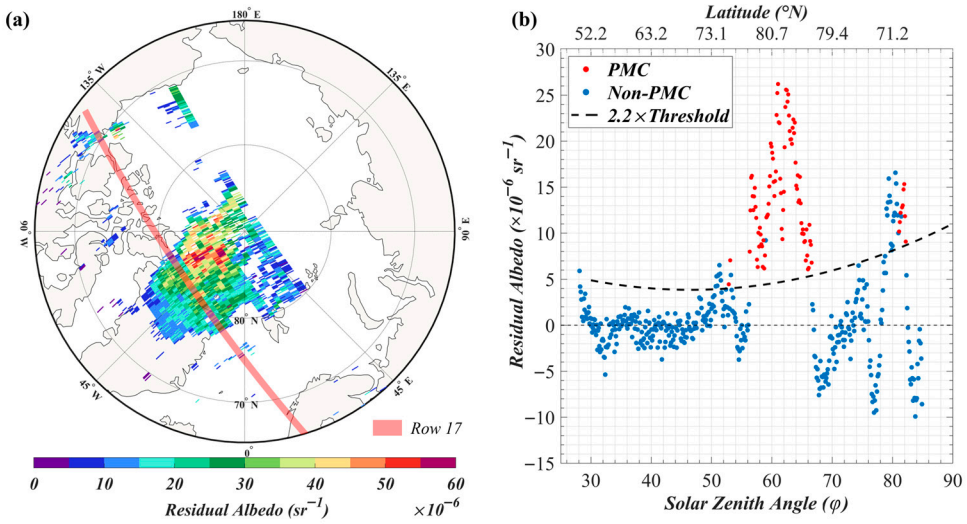


Figure 7. (**a**) TROPOMI PMC residual albedo at 283.0 nm for orbit 03675, 29 June 2018. (**b**) Albedo variation with solar zenith angle for all 283.0 nm pixels in row 17 (binned) of orbit 03675 on 29 June 2018.

The PMC detection results for multiple consecutive orbits (03674–03679) are shown in Figure 8. Results indicate that PMCs are widely distributed in the high-latitude regions (≥60°) of the summer hemisphere. Even after boundary pixels are removed during preprocessing, TROPOMI still maintains a wide cross-track swath of about 2300 km, allowing each orbit to extend close to the pole (90°). This effectively compensates for the limitations of satellites such as AIM/CIPS and S-NPP/OMPS-NP, which cannot observe the region very near the pole (>87°).

In terms of horizontal structure, PMC activity intensity within a single orbit shows no clear monotonic dependence on latitude. As shown in Figure 8 (Orbit 03677), PMC activity between 65° and 75°N and 45–60°W is stronger and more extensive than that at higher latitudes (>80°) within the same orbit. This phenomenon may result from regional differences in atmospheric conditions, including temperature, water vapor, and condensation nucleus concentration. Similar behavior has also been reported from OMI [14] and CIPS [50].

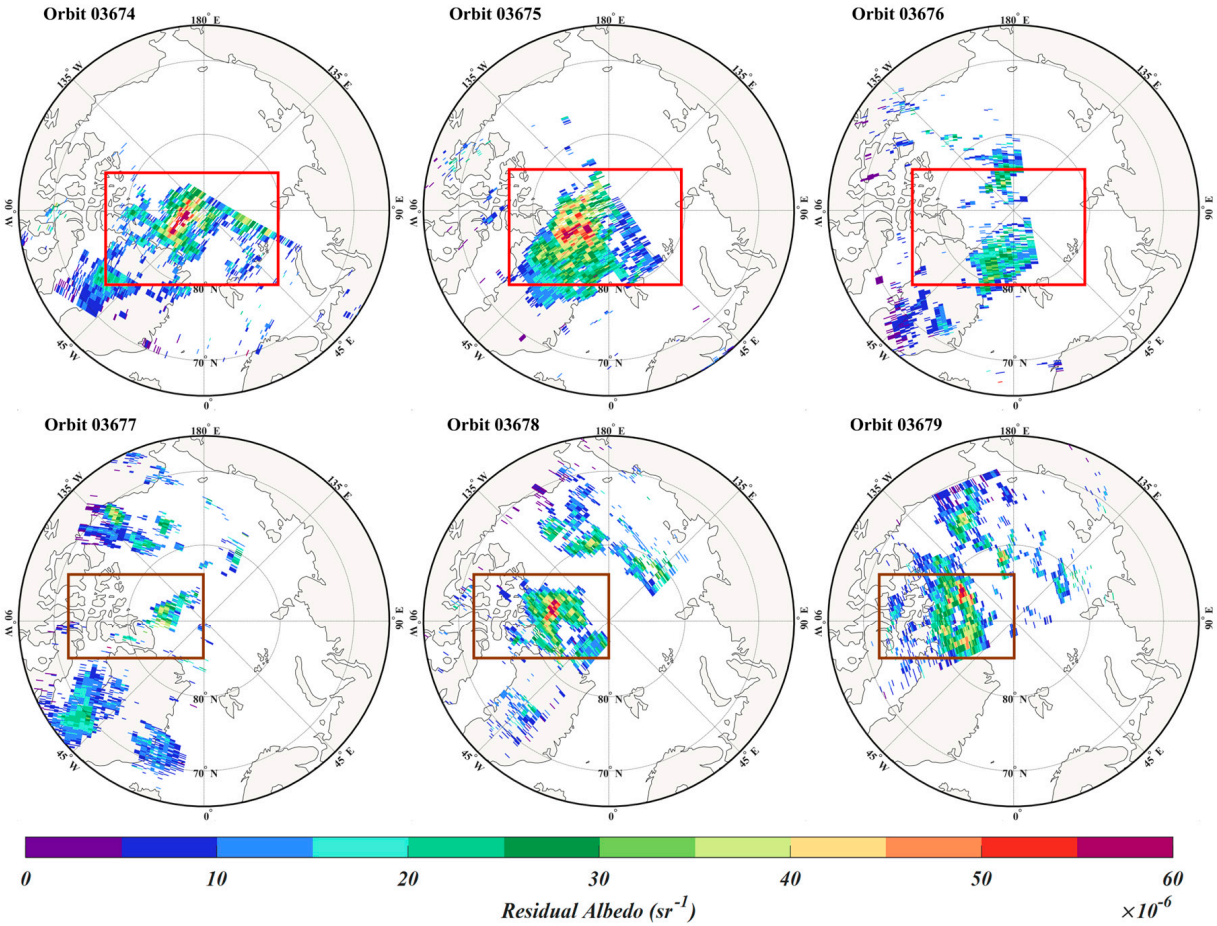


Figure 8. PMC detection results for consecutive TROPOMI orbits from 03674 to 03679.

In addition, the wide TROPOMI swath leads to substantial overlap in spatial coverage among adjacent orbits, enabling quasi-continuous observation of high-latitude regions through repeated coverage by consecutive orbits. In the results for orbits 03674–03676 (Top panel of Figure 8), the PMC activity in the red-boxed region expands from near the pole to 75°N and then rapidly weakens. Immediately afterward, in the brown-boxed region of orbits 03674–03676 (Bottom panel of Figure 8), PMC activity gradually intensifies and expands from near the pole to 70°N. These continuous observations indicate that TROPOMI can support studies of PMC activity on hourly timescales.

Figure 9 shows the seasonal distribution patterns of PMCs in the Northern and Southern Hemispheres in 2018. In contrast to the single-orbit scale, PMCs demonstrate pronounced latitude and temporal dependencies at a broader seasonal scale. Approximately 20 days prior to summer solstice, environmental alterations within the mesosphere facilitate the formation of polar mesospheric clouds, reaching a peak between +10 and +40 days. Thereafter, with the elevation of mesopause temperature, the activity of PMCs gradually diminishes [51].

3.2. Validation

3.2.1. Comparison with CIPS: Spatial Consistency

To characterize the horizontal variability of PMCs at the hemispheric scale, we project the calculated residual albedos from all orbits on a single day onto a uniform grid covering the summer hemisphere. The spatial resolution of the grid is 7.5 km × 7.5 km, consistent with CIPS L3A. If multiple orbits overlap, the brightest pixel (with the highest residual albedo) is used. The result is shown in Figure 10.

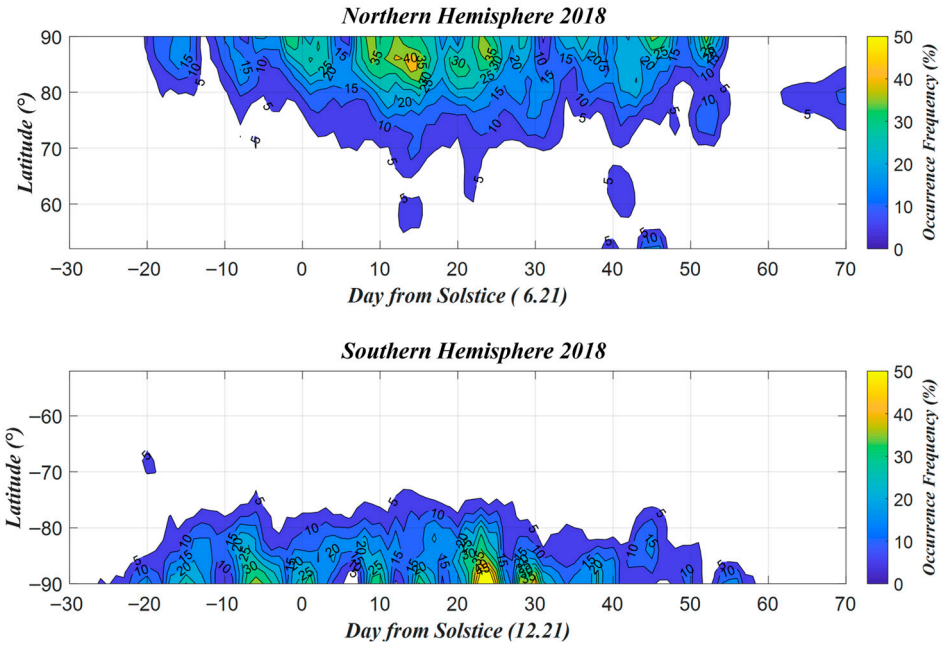


Figure 9. Daily zonal mean occurrence frequency of PMC in 2018. Occurrence frequencies (%) are calculated as the number of measurements identified as clouds relative to the total number of measurements in 2° latitude bins. All values are smoothed with a 3-day window.

Unlike single-orbit snapshots, which are sensitive to local environmental disturbances, the daily composite reveals more distinct large-scale activity patterns. The merged daily data show that PMCs are widely distributed around the pole and that the bright regions (high albedo) are mainly located between 70°N and 85°N. Note that the TROPOMI results do not show stronger PMC activity near the pole than in the lower-latitude band of 70°N–85°N (e.g., on days 5, 6, and 8). This feature will be investigated in future work.

In addition to visual comparison, we employed correlation coefficients, IoU, and FSS metrics (discussed in Section 2.2.5) to quantitatively analyze the spatial correlation between TROPOMI and CIPS; the results are presented in Figure 11. The average Pearson/Spearman correlation coefficients were 0.387 and 0.378, while the average IoU/FSS metrics were 0.756 and 0.928, respectively. Given the different spatiotemporal sampling, the relatively low pixel-by-pixel correlation coefficients between CIPS and TROPOMI are expected. The IoU and FSS metrics demonstrate that TROPOMI and CIPS exhibit consistent structural similarity within the latitude band of 70–85°N.

The comparison with CIPS suggests that the hemispheric horizontal distribution of PMCs may be influenced by persistent large-scale factors. Because of orbital differences, observations by CIPS and TROPOMI at the same latitude in the summer hemisphere are separated by 1 to 6 h. In the Northern Hemisphere, for example, CIPS primarily observes the polar region in the afternoon (LT 13-18), whereas TROPOMI observes it in the morning (LT 8-12). This difference precludes direct comparison under identical spatiotemporal conditions. Nevertheless, the continuous PMC observations from 15 to 24 June 2019 shown in Figure 10 indicate similar large-scale horizontal patterns in the CIPS and TROPOMI retrievals. The bright PMC regions (marked by red dashed boxes) show an apparent westward phase progression around the pole on daily timescales, with a period of about 5 days. This consistency indicates that, alongside rapidly fluctuating local conditions such as temperature, water vapor, and condensation nucleus concentration, longer-lived and larger-scale processes in the middle and upper atmosphere can modulate PMC activity on daily timescales.

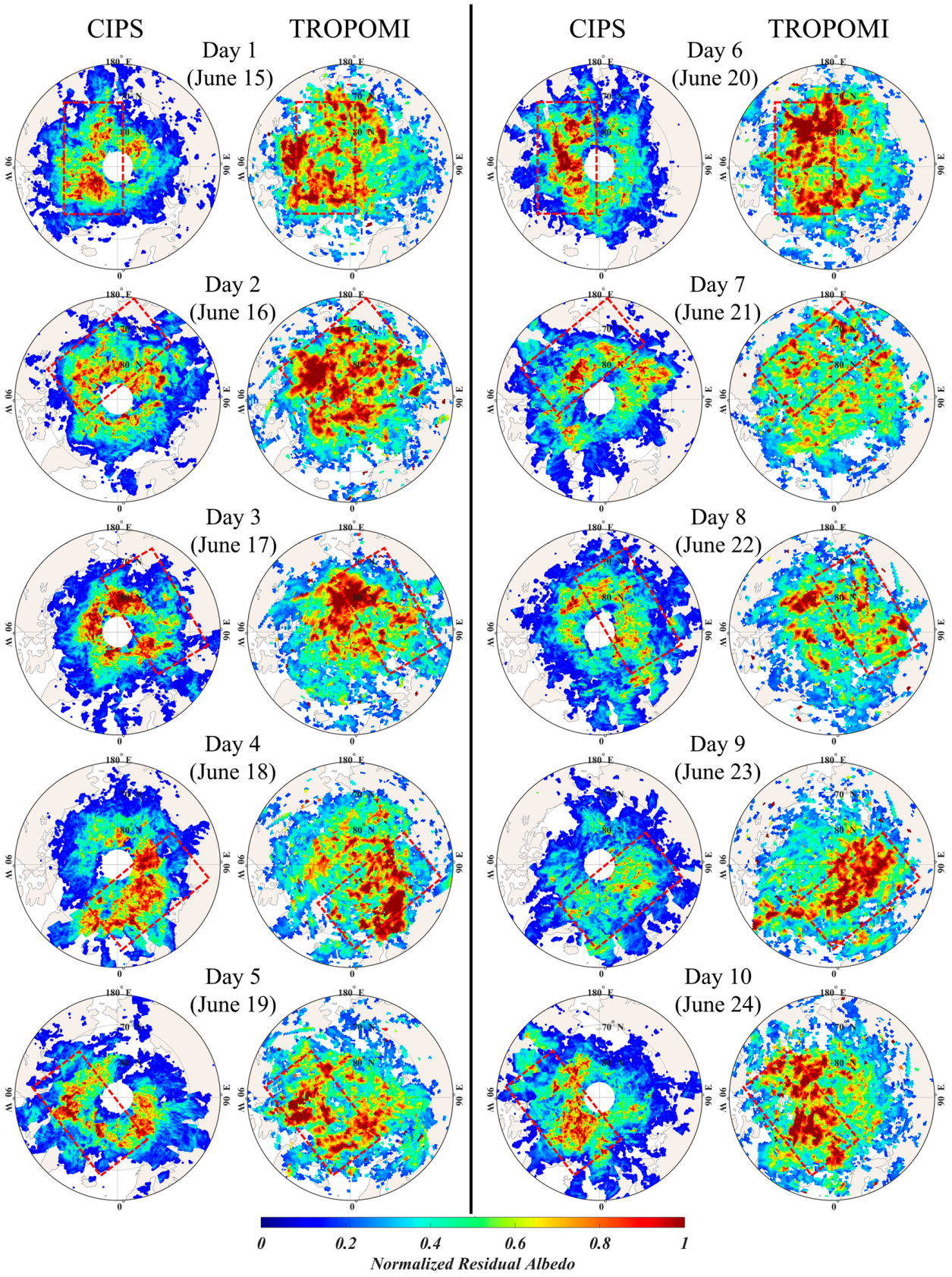


Figure 10. A 10-day sequence of normalized residual albedo of PMCs detected by TROPOMI and CIPS from 15 to 24 June 2019. Both datasets are projected into consistent 50 km × 50 km grid. The residual albedo values from CIPS and TROPOMI are normalized by dividing by 60×10^{-6} sr^{-1} and 30×10^{-6} sr^{-1}, respectively.

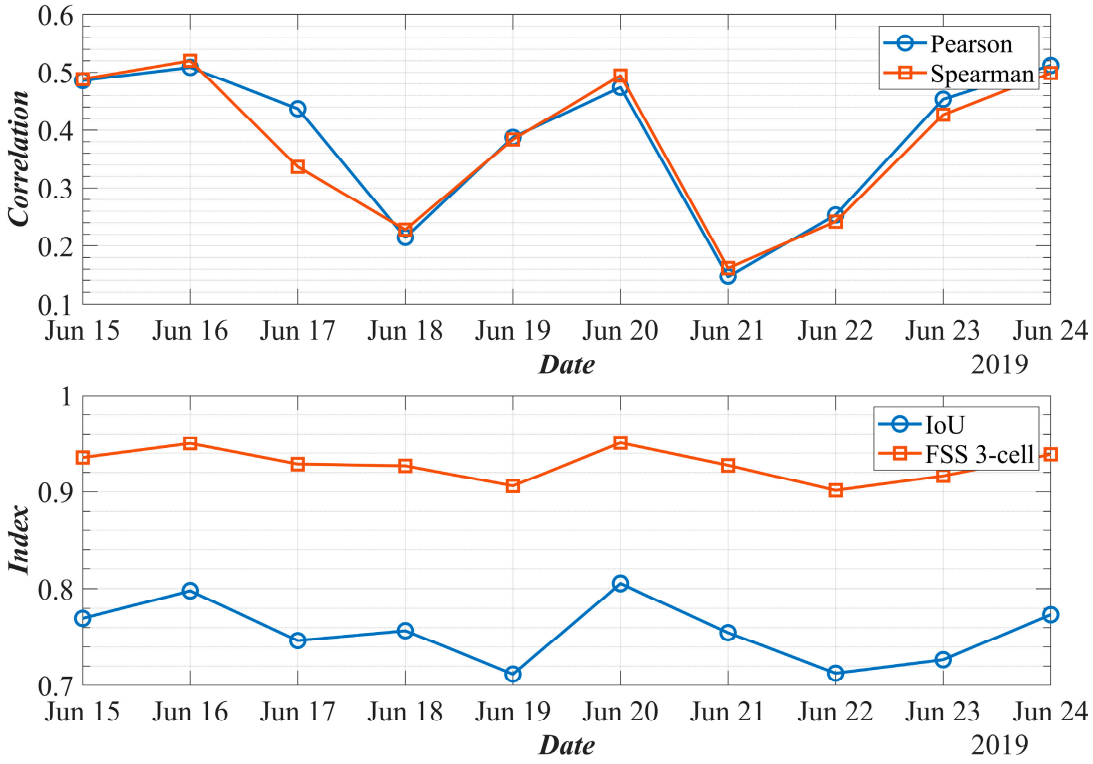


Figure 11. Statistical analysis of spatial correlation between CIPS and TROPOMI data from 15 June 2019, to 24 June 2019.

Previous studies [52] have shown that the thermal and dynamical state of the mesopause region is strongly controlled by wave activity. By modifying atmospheric conditions such as temperature and water vapor along the propagation path, waves can effectively modulate PMC occurrence, disappearance, brightness, altitude, and ice particle size. As shown in Figure 12, the longitude–time distribution exhibits an apparent westward phase progression with an approximately 5-day period and a dominant zonal wavenumber of 1. This pattern is consistent with possible quasi-5-day planetary-wave modulation; however, because TROPOMI and CIPS sample different local times and this study does not use coincident wind, temperature, or water-vapor diagnostics, we do not make a definitive dynamical attribution. Long-term and large-scale PMC horizontal structures may help characterize gravity waves [53], planetary waves [51], and other wave phenomena in the background atmosphere [27]. The high spatial resolution and daily global coverage of TROPOMI therefore provide a valuable new approach for studying wave–mesosphere interactions using PMC datasets.

3.2.2. Comparison with OMPS-NP: Quantitative Validation

Because OMPS-NP and TROPOMI are closely matched in both space and time, OMPS-NP data are used for quantitative validation based on residual albedo. The OMPS-NP pixel is much larger than the TROPOMI pixel, with one OMPS-NP pixel containing approximately 70 binned TROPOMI pixels, and this spatial difference results in varying viewing geometry among the TROPOMI pixels. As discussed in Section 2.2.1, we compute the area-weighted mean residual albedo of all TROPOMI pixels within each OMPS-NP pixel using Equation (1).

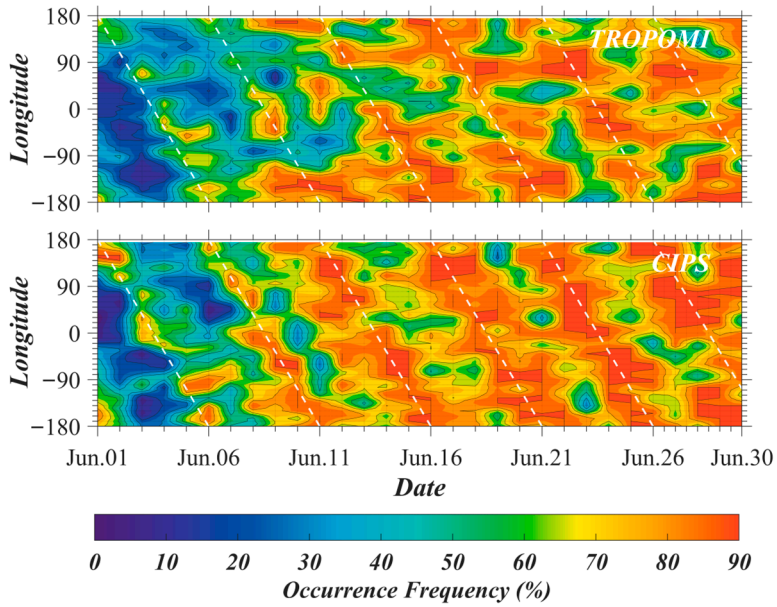


Figure 12. Longitudinal distribution of the daily occurrence frequency of TROPOMI and CIPS observations within the 70–85°N latitude range in the Northern Hemisphere, spanning the period from 1 June 2019, to 21 June 2019. Frequency values are smoothed with a 20° longitude window. The white dashed line represents an approximate five-day fluctuation structure.

For a single orbit, the comparison is shown in Figure 13. OMPS-NP pixels outlined in red are identified as PMCs in the OMPS-NP data, whereas pixels outlined in black represent the background atmosphere without PMCs (Figure 13a). Although the OMPS-NP swath is much narrower than that of TROPOMI, the overlapping region still shows a high degree of consistency. We categorize OMPS-NP pixels into three types: (1) pixels identified as non-cloud by OMPS-NP (Type 1); (2) pixels identified as cloud by OMPS-NP, where the ratio of TROPOMI cloud pixels within the pixel relative to all TROPOMI pixels is greater than 0.5 (Type 2); and (3) pixels identified as cloud by OMPS-NP, where the ratio of TROPOMI cloud pixels within the pixel relative to all TROPOMI pixels is less than 0.5 (Type 3). In the region of strong PMC activity (Type 2), both TROPOMI and OMPS-NP effectively distinguish PMCs from the background atmosphere, and the residual albedo of the OMPS-NP cloud pixels is consistent with the corresponding mean residual albedo from TROPOMI (yellow square in Figure 13b). This indicates that, for strong PMC activity, TROPOMI and OMPS-NP have comparable detection capability. Moreover, since the ratio of TROPOMI cloud pixels within OMPS-NP pixels exceeds 0.5, the suppressive effect of TROPOMI non-cloud pixels on the average albedo value is minimized. In contrast, in regions where the ratio of TROPOMI cloud pixels within OMPS-NP pixels is less than 0.5, non-cloud pixels significantly reduce the mean residual albedo value, as the expected value of the residual albedo for non-cloud pixels is 0.

Furthermore, all 14 TROPOMI orbits (03670–03683) on 29 June 2018, along with the corresponding OMPS-NP data, are analyzed (Figure 14). The multi-orbit composite indicates that TROPOMI and OMPS-NP possess comparable detection capabilities for strong PMC activity. For weaker PMCs, local agreement can decrease after TROPOMI pixels are averaged to the much coarser OMPS-NP footprint. This does not imply that TROPOMI is intrinsically less sensitive to PMCs. Rather, its finer spatial resolution enables it to detect smaller-scale PMC features, but the presence of background pixels reduces the mean residual albedo of TROPOMI during spatial averaging, which must be taken into account when making comparisons.

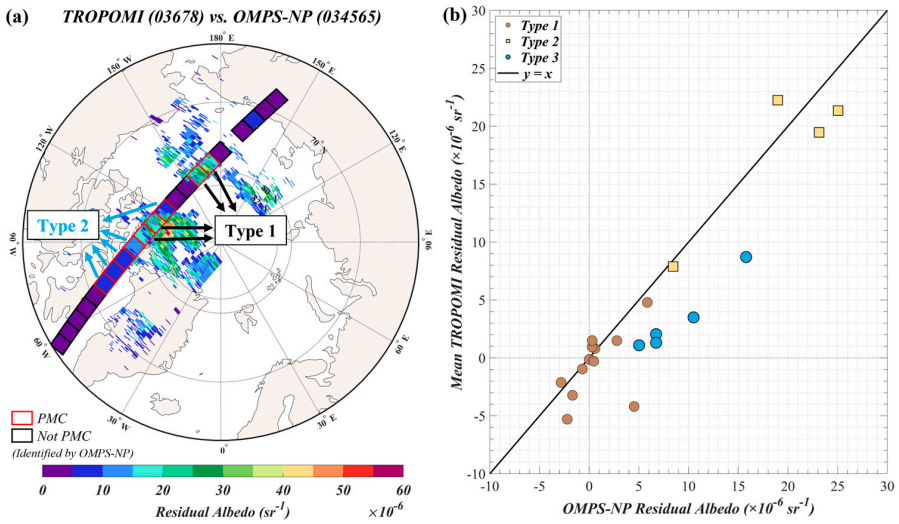


Figure 13. Comparison between TROPOMI (orbit 03678) and OMPS-NP (orbit 034565) residual albedos at 283.0 nm. (**a**) PMC detection results from TROPOMI and OMPS-NP; (**b**) Corresponding residual albedo values of pixels identified by OMPS-NP.

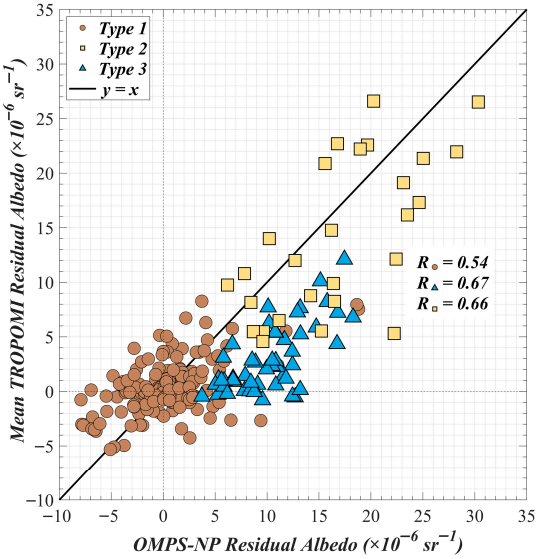


Figure 14. Comparison between TROPOMI and OMPS-NP residual albedos at 283.0 nm on 29 June 2018.

Correlations between TROPOMI and OMPS-NP were calculated for the three pixel types described above. For Type 1, the residual albedo of both OMPS-NP and TROPOMI is dominated by atmospheric variability and instrument noise, leading to weak correlation. For Types 2 and 3, the detection results from TROPOMI and OMPS-NP exhibit higher consistency, despite the varying decrease in the average TROPOMI albedo caused by background pixels.

3.2.3. Seasonal and Interannual Variation

Figure 15 shows the temporal variation in PMC occurrence frequency detected by TROPOMI, CIPS, and OMPS-NP in both hemispheres during 2018. In the Northern Hemisphere (Figure 15a), all three instruments record a decrease in PMC activity near day +33. In the Southern Hemisphere (Figure 15b), a similar decrease occurs near day +3. To align the TROPOMI results with those from CIPS and OMPS-NP, the Northern Hemisphere occurrence frequencies from CIPS and OMPS-NP are both multiplied by a scaling factor of

0.5. Because of differences in satellite orbits, instrument sensitivity, and sampling strategy, close numerical agreement in large-scale PMC occurrence frequency is not essential and can be adjusted relatively easily by modifying the detection threshold [23,32]. Therefore, the consistency in temporal variability demonstrates the reliability of the TROPOMI-based PMC detection.

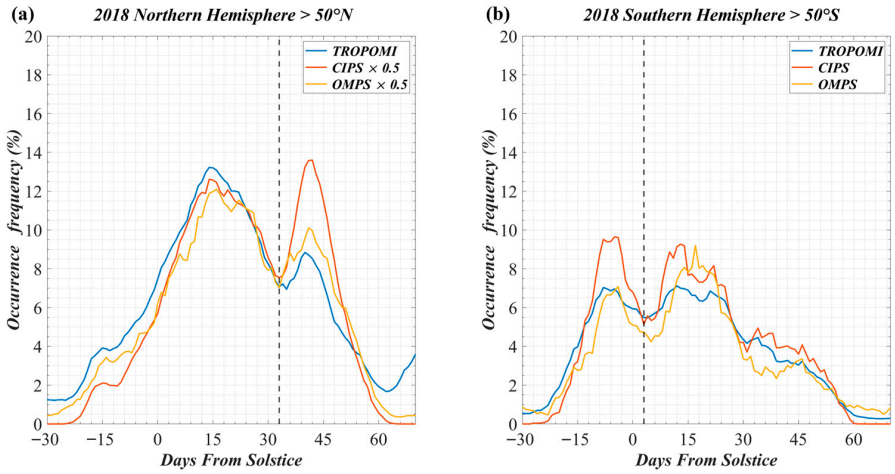


Figure 15. (**a**) Occurrence frequency of PMC activity in the Northern Hemisphere during the summer of 2018. (**b**) Occurrence frequency of PMC activity in the Southern Hemisphere during the summer of 2018. All values are smoothed with a 7-day window. The dash lines denote for day +33 and +3 day in Northern and southern hemisphere respectively.

Figure 16 shows the variation in PMC occurrence frequency from May 2018 to March 2023 as observed by TROPOMI, CIPS, and OMPS-NP. As in the single-year statistics shown in Figure 15, the three datasets remain broadly consistent over the longer time series. The results indicate that PMC activity is substantially stronger in the Northern Hemisphere than in the Southern Hemisphere. During the Southern Hemisphere season of 2019/2020 (November 2019–March 2020), however, the occurrence frequencies derived from CIPS and OMPS-NP increase markedly and greatly exceed those in other years, whereas the TROPOMI-based statistics do not show the same anomalous increase. Differences in observing mode and instrument performance may explain this discrepancy.

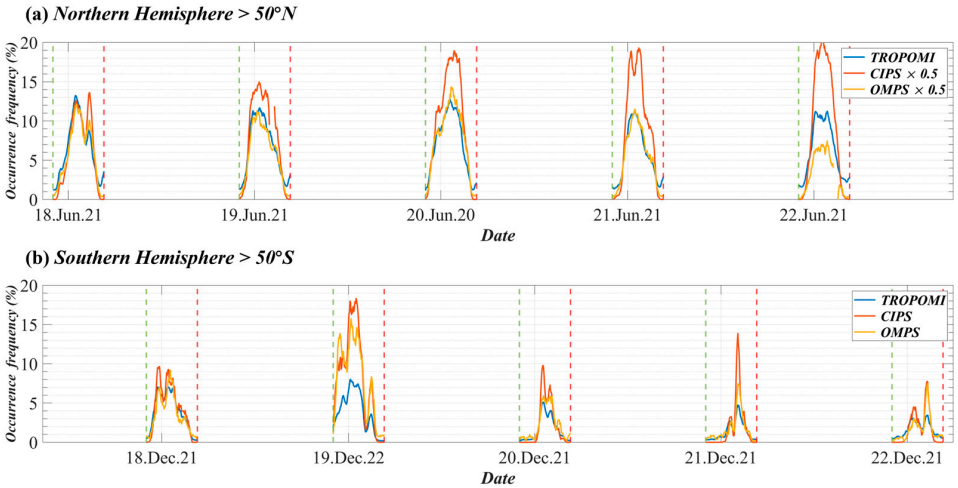


Figure 16. (**a**) Occurrence frequency of PMC activity in the Northern Hemisphere during the summers from 2018 to 2022. (**b**) Same as (**a**), but for the Southern Hemisphere. The red and green dashed lines represent the frequencies in the 30 days before (−30) and 70 days after (+70) the summer solstice, respectively. All values smoothed with a 7-day window.

4. Discussion

4.1. Algorithm Performance and Methodological Implications

The results demonstrate that the adapted SBUV-type algorithm can be successfully extended to hyperspectral nadir observations from TROPOMI, enabling robust PMC detection under strong Rayleigh-scattering conditions. The combination of optimized wavelength selection, iterative background fitting, and adaptive thresholding substantially improves detection sensitivity relative to more conventional approaches.

A key methodological advance lies in balancing signal enhancement against noise suppression in the UV1 band. By excluding wavelengths below 280 nm, where instrumental noise and calibration uncertainty increase rapidly, the algorithm avoids systematic bias while retaining sufficient sensitivity to PMC scattering. This result highlights the importance of instrument-specific optimization when adapting legacy algorithms to next-generation sensors.

Furthermore, the use of area-weighted spatial binning and geometric normalization ensures that the retrieved albedo remains physically consistent across varying viewing geometries. This is especially important for wide-swath instruments such as TROPOMI, for which cross-track changes in viewing angle can introduce non-negligible radiometric differences.

4.2. Multi-Scale Variability

The observed variability of PMCs across orbital and daily scales provides insight into the atmospheric processes that control PMC formation.

At orbital scales, the strong spatial heterogeneity and the absence of a monotonic dependence on latitude in individual-orbit snapshots are consistent with the influence of localized thermodynamic and dynamical variability, including mesopause temperature minima, water-vapor availability, vertical motion, background wind, condensation nuclei, and gravity-wave-induced cooling. These controlling factors are not directly retrieved from TROPOMI UV1 observations, so the interpretation remains qualitative.

At daily timescales, coherent large-scale structures, including the westward-propagating quasi-5-day pattern, suggest possible modulation by planetary-wave dynamics. Independent temperature, water-vapor, and wind diagnostics are needed to confirm the dynamical mechanism.

4.3. Inter-Instrument Consistency and Resolution Effects

The comparison with CIPS and OMPS-NP highlights both the strengths and the limitations of TROPOMI observations.

The strong agreement with OMPS-NP in regions of intense PMC activity confirms that TROPOMI is broadly consistent with long-term SBUV-type datasets, thereby supporting compatibility with existing climatological records. At the same time, the higher spatial resolution of TROPOMI enables detection of fine-scale structures that are unresolved by OMPS-NP.

The discrepancies observed in weak-signal regions can be interpreted as a consequence of sub-pixel variability. Whereas OMPS-NP provides spatially averaged measurements over large footprints, TROPOMI resolves heterogeneous cloud fields within those footprints. This difference underscores the importance of accounting for spatial resolution when comparing datasets and suggests that TROPOMI may better represent small-scale PMC occurrence.

The agreement with CIPS in capturing planetary-scale structures further supports the reliability of TROPOMI for high-resolution PMC studies despite differences in local-time sampling.

4.4. Limitations and Uncertainties

Despite the overall robustness of the proposed method, several limitations should be acknowledged.

1. The use of a single-scattering approximation in the Rayleigh background modeling neglects possible contributions from multiple scattering, particularly at large solar zenith angles and for the 295.0 and 298.0 nm channels. Although previous studies suggest that this effect is small in the ultraviolet, it may still introduce systematic bias under some conditions.
2. The polynomial fitting approach assumes a smooth dependence of albedo on solar zenith angle and may not fully capture complex atmospheric variability. Although the iterative cloud-removal scheme mitigates this issue, some uncertainty in background estimation remains. A reliable radiative-transfer model coupled with precise atmospheric parameters could further enhance the modeling effectiveness of the Rayleigh background [40].
3. The adaptive thresholding method relies on off-season data to characterize noise levels. Any seasonal changes in instrument performance or atmospheric state may therefore influence the accuracy of the threshold determination.
4. The geometric normalization depends on assumed particle properties, such as effective radius and shape. Variations in PMC microphysics may introduce additional uncertainty into the corrected albedo. The Ångström exponent may provide a path for hyperspectral instruments to constrain particle-size effects [1,14].
5. Quantitative sensitivity tests were added to bound the main algorithmic uncertainties summarized below (Table 2). They show that cloud occurrence is comparatively robust to polynomial order and radius assumptions, whereas absolute normalized albedo is more sensitive to the assumed particle radius and large-SZA retrievals remain less certain.

Table 2. Summary of main algorithm-sensitivity tests and uncertainty implications.

Uncertainty Source	Sensitivity Test	Result
Polynomial-order choice	p = 3, 4, 5, 6 using order-specific threshold	Occurrence changes of −1.126, −1.206, and −1.637 percentage points relative to p = 4
Adaptive threshold factor	c = 1.6–2.8 for the 29 June 2018 full-day sample	Occurrence changes from +4.082 to −2.878 percentage points relative to c = 2.2
Particle-radius assumption	Angular normalization repeated for radii of 20–80 nm	Normalized albedo changes from +27.1% to −54.3% relative to r = 40 nm

4.5. Implications for Long-Term PMC Monitoring

The discontinuation of the CIPS mission has created a significant gap in high-resolution PMC observations. The results of this study demonstrate that TROPOMI can partially fill this gap by providing continuous, high-resolution, and globally consistent measurements.

By bridging the spatial-resolution gap between OMPS-NP and CIPS, TROPOMI offers a valuable opportunity to extend PMC climate records into a new observational era. This capability is particularly important for detecting long-term trends and improving our understanding of how the mesosphere responds to climate change. The high spatial resolution of TROPOMI also opens new possibilities for investigating mesospheric dynamics, including gravity-wave propagation and wave-mean-flow interactions, which remain poorly constrained by existing observations.

Future work should focus on integrating TROPOMI-derived PMC datasets with numerical models and complementary satellite observations to further improve under-

standing of mesospheric processes and their role in Earth's climate system. Furthermore, more quantitative criteria for characteristic band selection, as well as a particle radius retrieval method based on the Ångström exponent, can also help extend the scope of TROPOMI applications.

5. Conclusions

We present the first systematic PMC detection using Sentinel-5P/TROPOMI data and demonstrate its potential as a high-resolution nadir-viewing sensor for PMC research. By extending the SBUV-type framework to hyperspectral ultraviolet observations with optimized wavelength selection, iterative background fitting, and adaptive thresholding, we reliably separate weak PMC signals from the background atmosphere.

Relative to operational OMPS-NP, the higher spatial resolution of TROPOMI resolves finer small-scale structures and helps fill the gap left by the end of AIM/CIPS operations in March 2023. After binning, the ~2300 km swath provides broad coverage of mid- and high latitudes and reduces the polar coverage gap of CIPS and OMPS-NP. Comparisons with OMPS-NP and CIPS show that TROPOMI is broadly consistent with existing PMC observations. In particular, TROPOMI and CIPS show a westward wave-like modulation consistent with possible quasi-5-day planetary-wave influence, whereas the close agreement in residual albedo with OMPS-NP supports the reliability of the retrieval. Multi-scale analyses further indicate that orbital-scale PMC variability is consistent with local thermodynamic and dynamical variability and that daily-scale variability may be modulated by larger-scale waves. These results are consistent with previous observations and support the robustness of the TROPOMI retrievals.

Overall, TROPOMI provides an effective balance between spatial resolution and global coverage, forming a key link between traditional long-term records and high-resolution PMC observations. Following the end of the CIPS mission, it offers important continuity for PMC climate studies and supplies a valuable new observational basis for investigating mesospheric dynamics and climate variability.

Author Contributions: Funding acquisition, S.G.; investigation, W.W. and S.G.; methodology, W.W. and S.G.; project administration, S.G.; software, W.W.; writing—original draft preparation, W.W.; writing—review and editing, S.G., Y.Q., Y.W. (Yafei Wei), Z.W., Y.Q., X.H. and Y.W. (Yongmei Wang) All authors have read and agreed to the published version of the manuscript.

Funding: This work was supported by the National Natural Science Foundation of China (Grant 42374195), Natural Science Foundation of Wuhan (Grant 2025041001010362) and the Fundamental Research Funds for the Central Universities (242025kf0035).

Data Availability Statement: TROPOMI L1B data are available from the Copernicus Data Space Ecosystem (https://dataspace.copernicus.eu/) (accessed on 28 March 2026). CIPS data are available at https://lasp.colorado.edu/aim/ (accessed on 28 March 2026). OMPS-NP data are available at http://sbuv.gsfc.nasa.gov/pmc/v4/ (accessed on 28 March 2026).

Acknowledgments: We thank the AIM/CIPS team for their sustained efforts in providing CIPS PMC data and Matthew T. DeLand for making the processed OMPS-NP PMC data publicly available.

Conflicts of Interest: The authors declare no conflicts of interest.

References

1. von Savigny, C. On the retrieval of particle size information of noctilucent clouds from optical remote sensing measurements. *J. Atmos. Sol.-Terr. Phys.* **2025**, *269*, 106447. [CrossRef]
2. DeLand, M.T.; Shettle, E.P.; Thomas, G.E.; Olivero, J.J. A quarter-century of satellite polar mesospheric cloud observations. *J. Atmos. Sol.-Terr. Phys.* **2006**, *68*, 9–29. [CrossRef]

3. Pan, W. The First Ground-based Lidar Measurement of Noctilucent Clouds over Tibetan Plateau. In Proceedings of the AGU Fall Meeting Abstracts, Washington, DC, USA, 10–14 December 2018.
4. Dalin, P.; Suzuki, H.; Pertsev, N.; Perminov, V.; Shevchuk, N.; Tsimerinov, E.; Zalcik, M.; Brausch, J.; McEwan, T.; McEachran, I.; et al. The strong activity of noctilucent clouds at middle latitudes in 2020. *Polar Sci.* **2023**, *35*, 100920. [CrossRef]
5. Thomas, G.E.; Olivero, J. Noctilucent clouds as possible indicators of global change in the mesosphere. *Adv. Space Res.* **2001**, *28*, 937–946. [CrossRef]
6. Lübken, F.J.; Berger, U.; Baumgarten, G. On the Anthropogenic Impact on Long-Term Evolution of Noctilucent Clouds. *Geophys. Res. Lett.* **2018**, *45*, 6681–6689. [CrossRef]
7. Wallis, S.; DeLand, M.; von Savigny, C. Did the 2022 Hunga eruption impact the noctilucent cloud season in 2023/24 and 2024? *Atmos. Chem. Phys.* **2025**, *25*, 3635–3645. [CrossRef]
8. Donahue, T.M.; Guenther, B.; Blamont, J.E. Noctilucent Clouds in Daytime: Circumpolar Particulate Layers Near the Summer Mesopause. *J. Atmos. Sci.* **1972**, *29*, 1205–1209. [CrossRef]
9. Petelina, S.V.; Degenstein, D.A.; Llewellyn, E.J.; Lloyd, N.D.; Mertens, C.J.; Mlynczak, M.G.; Russell, J.I.I.I. Thermal conditions for PMC existence derived from Odin/OSIRIS and TIMED/SABER data. *Geophys. Res. Lett.* **2005**, *32*, L17813. [CrossRef]
10. von Savigny, C.; Kokhanovsky, A.; Bovensmann, H.; Eichmann, K.U.; Kaiser, J.; Noël, S.; Rozanov, A.V.; Skupin, J.; Burrows, J.P. NLC detection and particle size determination: First results from SCIAMACHY on ENVISAT. *Adv. Space Res.* **2004**, *34*, 851–856. [CrossRef]
11. DeLand, M.T.; Gorkavyi, N. PMC observations from the OMPS Limb Profiler. *J. Atmos. Sol.-Terr. Phys.* **2021**, *213*, 105505. [CrossRef]
12. Thomas, G.E.; Mcpeters, R.D.; Jensen, E.J. Satellite-Observations of Polar Mesospheric Clouds by the Solar Backscattered Ultraviolet Spectral Radiometer—Evidence of a Solar-Cycle Dependence. *J. Geophys. Res.-Atmos.* **1991**, *96*, 927–939. [CrossRef]
13. Shettle, E.P.; DeLand, M.T.; Thomas, G.E.; Olivero, J.J. Long term variations in the frequency of polar mesospheric clouds in the Northern Hemisphere from SBUV. *Geophys. Res. Lett.* **2009**, *36*, L02803. [CrossRef]
14. DeLand, M.T.; Shettle, E.P.; Levelt, P.F.; Kowalewski, M.G. Polar mesospheric clouds (PMCs) observed by the Ozone Monitoring Instrument (OMI) on Aura. *J. Geophys. Res.-Atmos.* **2010**, *115*, D21301. [CrossRef]
15. DeLand, M.T.; Thomas, G.E. Extending the SBUV polar mesospheric cloud data record with the OMPS NP. *Atmos. Chem. Phys.* **2019**, *19*, 7913–7925. [CrossRef]
16. Hervig, M.E.; Gordley, L.L.; Deaver, L.E.; Siskind, D.E.; Stevens, M.H.; Russell, J.M.; Bailey, S.M.; Megner, L.; Bardeen, C.G. First Satellite Observations of Meteoric Smoke in the Middle Atmosphere. *Geophys. Res. Lett.* **2009**, *36*, L18805. [CrossRef]
17. Hervig, M.E.; Gordley, L.L.; Russell, J.M.; Bailey, S.M. SOFIE PMC observations during the northern summer of 2007. *J. Atmos. Sol.-Terr. Phys.* **2009**, *71*, 331–339. [CrossRef]
18. Stevens, M.H.; Conway, R.R.; Englert, C.R.; Summers, M.E.; Grossmann, K.U.; Gusev, O.A. PMCs and the water frost point in the Arctic summer mesosphere. *Geophys. Res. Lett.* **2001**, *28*, 4449–4452. [CrossRef]
19. O'Neil, R.R.; Richards, E.; Humphrey, C.H.; Stair, A.T. Polar mesospheric clouds: Infrared measurements from the Midcourse Space Experiment. *J. Geophys. Res.-Space Phys.* **2008**, *113*, A07303. [CrossRef]
20. Kumar, V.R.; Collins, R.L.; Li, J.T.; Kerven, R.; Alspach, J.; Thorsen, D. An extended investigation of noctilucent cloud dynamics at Chatanika, Alaska using lidar, satellite, and radar observations. *J. Atmos. Sol.-Terr. Phys.* **2026**, *280*, 106764. [CrossRef]
21. Gao, H.Y.; Shepherd, G.G.; Tang, Y.H.; Bu, L.B.; Wang, Z. Double-layer structure in polar mesospheric clouds observed from SOFIE/AIM. *Ann. Geophys.* **2017**, *35*, 295–309. [CrossRef]
22. DeLand, M.T.; Thomas, G.E. Evaluation of Space Traffic Effects in SBUV Polar Mesospheric Cloud Data. *J. Geophys. Res.-Atmos.* **2019**, *124*, 4203–4221. [CrossRef]
23. DeLand, M.T.; Thomas, G.E. Updated PMC trends derived from SBUV data. *J. Geophys. Res.-Atmos.* **2015**, *120*, 2140–2166. [CrossRef]
24. DeLand, M.T.; Shettle, E.P.; Thomas, G.E.; Olivero, J.J. Solar backscattered ultraviolet (SBUV) observations of polar mesospheric clouds (PMCs) over two solar cycles. *J. Geophys. Res.-Atmos.* **2003**, *108*, 8445. [CrossRef]
25. Eckermann, S.D.; Hoppel, K.W.; Coy, L.; McCormack, J.P.; Siskind, D.E.; Nielsen, K.; Kochenash, A.; Stevens, M.H.; Englert, C.R.; Singer, W.; et al. High-altitude data assimilation system experiments for the northern summer mesosphere season of 2007. *J. Atmos. Sol.-Terr. Phys.* **2009**, *71*, 531–551. [CrossRef]
26. Dalin, P.; Pogoreltsev, A.; Pertsev, N.; Perminov, V.; Shevchuk, N.; Dubietis, A.; Zalcik, M.; Kulikov, S.; Zadorozhny, A.; Kudabayeva, D.; et al. Evidence of the formation of noctilucent clouds due to propagation of an isolated gravity wave caused by a tropospheric occluded front. *Geophys. Res. Lett.* **2015**, *42*, 2037–2046. [CrossRef]
27. Liu, X.; Yue, J.; Xu, J.Y.; Yuan, W.; Russell, J.M.; Hervig, M.E.; Nakamura, T. Persistent longitudinal variations in 8years of CIPS/AIM polar mesospheric clouds. *J. Geophys. Res.-Atmos.* **2016**, *121*, 8390–8409. [CrossRef]

28. Thurairajah, B.; Bailey, S.M.; Harvey, V.L.; Randall, C.E.; France, J.A. The Role of the Quasi 5-Day Wave on the Onset of Polar Mesospheric Cloud Seasons in the Northern Hemisphere. *J. Geophys. Res.-Atmos.* **2023**, *128*, e2022JD037982. [CrossRef]
29. Rong, P.P.; Yue, J.; Russell, J.M.; Lumpe, J.D.; Gong, J.; Wu, D.L.; Randall, C.E. Horizontal winds derived from the polar mesospheric cloud images as observed by the CIPS instrument on the AIM satellite. *J. Geophys. Res.-Atmos.* **2015**, *120*, 5564–5584. [CrossRef]
30. Lee, J.N.; Wu, D.L.; Thurairajah, B.; Hozumi, Y.; Tsuda, T. The Sensitivity of Polar Mesospheric Clouds to Mesospheric Temperature and Water Vapor. *Remote Sens.* **2024**, *16*, 1563. [CrossRef]
31. Zhang, L.; Tinsley, B.; Zhou, L.M. Responses of CIPS/AIM noctilucent clouds to the interplanetary magnetic field. *Atmos. Chem. Phys.* **2022**, *22*, 13355–13370. [CrossRef]
32. Langowski, M.P.; von Savigny, C.; Bachmann, T.; DeLand, M.T. First results on the retrieval of noctilucent cloud albedo and occurrence rate from SCIAMACHY/Envisat satellite nadir measurements. *J. Atmos. Sol.-Terr. Phys.* **2018**, *175*, 31–39. [CrossRef]
33. Schenkeveld, V.M.E.; Jaross, G.; Marchenko, S.; Haffner, D.; Kleipool, Q.L.; Rozemeijer, N.C.; Veefkind, J.P.; Levelt, P.F. In-flight performance of the Ozone Monitoring Instrument. *Atmos. Meas. Tech.* **2017**, *10*, 1957–1986. [CrossRef]
34. Veefkind, J.P.; Aben, I.; McMullan, K.; Förster, H.; de Vries, J.; Otter, G.; Claas, J.; Eskes, H.J.; de Haan, J.F.; Kleipool, Q.; et al. TROPOMI on the ESA Sentinel-5 Precursor: A GMES mission for global observations of the atmospheric composition for climate, air quality and ozone layer applications. *Remote Sens. Environ.* **2012**, *120*, 70–83. [CrossRef]
35. Sentinel-5P TROPOMI Level-1b Algorithm Technical Baseline Documentation. Available online: https://sentiwiki.copernicus.eu/web/document-library#DocumentLibrary-SENTINEL-5PDocumentsLibrary-S5P-Documents (accessed on 16 March 2026).
36. Sentinel-5P TROPOMI Level-1b Product Readme File. Available online: https://sentiwiki.copernicus.eu/web/s5p-products (accessed on 16 March 2026).
37. McClintock, W.E.; Rusch, D.W.; Thomas, G.E.; Merkel, A.W.; Lankton, M.R.; Drake, V.A.; Bailey, S.M.; Russell, J.M. The cloud imaging and particle size experiment on the Aeronomy of Ice in the mesosphere mission: Instrument concept, design, calibration, and on-orbit performance. *J. Atmos. Sol.-Terr. Phys.* **2009**, *71*, 340–355. [CrossRef]
38. Flynn, L.; Long, C.; Wu, X.; Evans, R.; Beck, C.T.; Petropavlovskikh, I.; McConville, G.; Yu, W.; Zhang, Z.; Niu, J.; et al. Performance of the Ozone Mapping and Profiler Suite (OMPS) products. *J. Geophys. Res.-Atmos.* **2014**, *119*, 6181–6195. [CrossRef]
39. Hughes, G. On the mean accuracy of statistical pattern recognizers. *IEEE Trans. Inf. Theory* **1968**, *14*, 55–63. [CrossRef]
40. Lumpe, J.D.; Bailey, S.M.; Carstens, J.N.; Randall, C.E.; Rusch, D.W.; Thomas, G.E.; Nielsen, K.; Jeppesen, C.; McClintock, W.E.; Merkel, A.W.; et al. Retrieval of polar mesospheric cloud properties from CIPS: Algorithm description, error analysis and cloud detection sensitivity. *J. Atmos. Sol.-Terr. Phys.* **2013**, *104*, 167–196. [CrossRef]
41. Mishchenko, M.I.; Travis, L.D.; Lacis, A.A. *Scattering, Absorption, and Emission of Light by Small Particles*; Cambridge University Press: Cambridge, UK, 2002.
42. Mishchenko, M.I.; Travis, L.D. Capabilities and limitations of a current FORTRAN implementation of the T-matrix method for randomly oriented, rotationally symmetric scatterers. *J. Quant. Spectrosc. Radiat. Transf.* **1998**, *60*, 309–324. [CrossRef]
43. Somerville, W.R.C.; Auguié, B.; Le Ru, E.C. SMARTIES: User-friendly codes for fast and accurate calculations of light scattering by spheroids. *J. Quant. Spectrosc. Radiat. Transf.* **2016**, *174*, 39–55. [CrossRef]
44. Bak, J.; Liu, X.; Abad, G.G.; Yang, K. An Extension of Ozone Profile Retrievals from TROPOMI Based on the SAO2024 Algorithm. *Remote Sens.* **2025**, *17*, 779. [CrossRef]
45. Ren, K.; Gao, H.Y.; Niu, S.Q.; Sun, S.Y.; Kou, L.L.; Xie, Y.Q.; Zhang, L.G.; Bu, L.B. Simulation and detection efficiency analysis for measurements of polar mesospheric clouds using a spaceborne wide-field-of-view ultraviolet imager. *Atmos. Meas. Tech.* **2024**, *17*, 4825–4842. [CrossRef]
46. Thomas, G.E.; Mckay, C.P. On the Mean Particle-Size and Water-Content of Polar Mesospheric Clouds. *Planet. Space Sci.* **1985**, *33*, 1209–1224. [CrossRef]
47. DeLand, M.T.; Shettle, E.P.; Thomas, G.E.; Olivero, J.J. Direct observations of PMC local time variations by Aura OMI. *J. Atmos. Sol.-Terr. Phys.* **2011**, *73*, 2049–2064. [CrossRef]
48. Ebert, E.E. Fuzzy verification of high-resolution gridded forecasts: A review and proposed framework. *Meteorol. Appl.* **2008**, *15*, 51–64. [CrossRef]
49. Roberts, N.M.; Lean, H.W. Scale-Selective Verification of Rainfall Accumulations from High-Resolution Forecasts of Convective Events. *Mon. Weather. Rev.* **2008**, *136*, 78–97. [CrossRef]
50. Thurairajah, B.; Bailey, S.M.; Nielsen, K.; Randall, C.E.; Lumpe, J.D.; Taylor, M.J.; Russell, J.M. Morphology of polar mesospheric clouds as seen from space. *J. Atmos. Sol.-Terr. Phys.* **2013**, *104*, 234–243. [CrossRef]
51. Merkel, A.W.; Rusch, D.W.; Palo, S.E.; Russell, J.M.; Bailey, S.M. Mesospheric planetary wave effects on global PMC variability inferred from AIM-CIPS and TIMED-SABER for the northern summer 2007 PMC season. *J. Atmos. Sol.-Terr. Phys.* **2009**, *71*, 381–391. [CrossRef]

52. France, J.A.; Randall, C.E.; Lieberman, R.S.; Harvey, V.L.; Eckermann, S.D.; Siskind, D.E.; Lumpe, J.D.; Bailey, S.M.; Carstens, J.N.; Russell, J.M., III. Local and Remote Planetary Wave Effects on Polar Mesospheric Clouds in the Northern Hemisphere in 2014. *J. Geophys. Res. Atmos.* **2018**, *123*, 5149–5162. [CrossRef]
53. Randall, C.E.; Carstens, J.; France, J.A.; Harvey, V.L.; Hoffmann, L.; Bailey, S.M.; Alexander, M.J.; Lumpe, J.D.; Yue, J.; Thurairajah, B.; et al. New AIM/CIPS global observations of gravity waves near 50–55 km. *Geophys. Res. Lett.* **2017**, *44*, 7044–7052. [CrossRef]

Disclaimer/Publisher's Note: The statements, opinions and data contained in all publications are solely those of the individual author(s) and contributor(s) and not of MDPI and/or the editor(s). MDPI and/or the editor(s) disclaim responsibility for any injury to people or property resulting from any ideas, methods, instructions or products referred to in the content.